

Research Paper

# Tuned near infrared fluorescent hyaluronic acid conjugates for delivery to pancreatic cancer for intraoperative imaging

Bowen Qi<sup>1</sup>, Ayrienne J. Crawford<sup>2</sup>, Nicholas E. Wojtynek<sup>2</sup>, Geoffrey A. Talmon<sup>3</sup>, Michael A. Hollingsworth<sup>2,4</sup>, Quan P. Ly<sup>4,5</sup>, Aaron M. Mohs<sup>1,5,6</sup>✉

1. Department of Pharmaceutical Sciences, University of Nebraska Medical Center, Omaha, Nebraska 68198, United States
2. Eppley Institute for Research in Cancer and Allied Diseases, University of Nebraska Medical Center, Omaha, Nebraska 68198, United States
3. Department of Pathology and Microbiology, University of Nebraska Medical Center, Omaha, Nebraska 68198, United States
4. Fred and Pamela Buffett Cancer Center, University of Nebraska Medical Center, Omaha, Nebraska 68198, United States
5. Department of Surgery, University of Nebraska Medical Center, Omaha, Nebraska 68198, United States
6. Department of Biochemistry and Molecular Biology, University of Nebraska Medical Center, Omaha, Nebraska 68198, United States

✉ Corresponding author: Aaron M. Mohs, Ph.D., Department of Pharmaceutical Sciences, Fred and Pamela Buffett Cancer Center, University of Nebraska Medical Center, 5.12.315 Scott Research Tower, Omaha, NE 68198-6858. Email: aaron.mohs@unmc.edu

© The author(s). This is an open access article distributed under the terms of the Creative Commons Attribution License (<https://creativecommons.org/licenses/by/4.0/>). See <http://ivyspring.com/terms> for full terms and conditions.

Received: 2019.09.26; Accepted: 2020.01.23; Published: 2020.02.10

## Abstract

The prognosis of pancreatic cancer remains poor. Intraoperative fluorescence imaging of tumors could improve staging and surgical resection, thereby improving prognosis. However, imaging pancreatic cancer with macromolecular delivery systems, is often hampered by nonspecific organ accumulation.

**Methods:** We describe the rational development of hyaluronic acid (HA) conjugates that vary in molecular weight and are conjugated to near infrared fluorescent (NIRF) dyes that have differences in hydrophilicity, serum protein binding affinity, and clearance mechanism. We systematically investigated the roles of each of these properties on tumor accumulation, relative biodistribution, and the impact of intraoperative imaging of orthotopic, syngeneic pancreatic cancer.

**Results:** Each HA-NIRF conjugate displayed intrapancreatic tumor enhancement. Regardless of HA molecular weight, Cy7.5 conjugation directed biodistribution to the liver, spleen, and bowels. Conjugation of IRDye800 to 5 and 20 kDa HA resulted in low liver and spleen signal while enhancing the tumor up to 14-fold compared to healthy pancreas, while 100 kDa HA conjugated to IRDye800 resulting in liver and spleen accumulation.

**Conclusion:** These studies demonstrate that by tuning HA molecular weight and the physicochemical properties of the conjugated moiety, in this case a NIRF probe, peritoneal biodistribution can be substantially altered to achieve optimized delivery to tumors intraoperative abdominal imaging.

Key words: Pancreatic ductal adenocarcinoma, hyaluronic acid, fluorescence guided surgery, biodistribution, serum protein binding

## Introduction

Surgical resection remains a promising treatment for improving prognosis of cancer patients as it is potentially curative for primary tumors and local metastases [1]. Currently, surgery is performed without contrast-enhanced image-guidance to

identify tumor margins and small occult metastases due to the absence of clinically available optical contrast agents [2]. Contrast-enhanced optical imaging could provide real-time guidance during tumor resection with sensitive, rapid, and

non-radioactive near-infrared fluorescent (NIRF) tracers to highlight the areas of extension of the malignancy [3–5]. NIRF is promising for *in vivo* optical imaging due the relative biological transparency at wavelengths between 700 and 1000 nm [2]. Fluorescence image-guided surgery (FIGS) has so far shown its potential to support surgical procedures and the feasibility to improve clinical outcomes [6–9]. However, FIGS of tumors has not reached its full potential, in part due to contrast agents lacking high intensity, water solubility, biocompatibility, and tissue-specific targetability [10].

Attaining high contrast-to-noise ratio (CNR: signal in region of interest relative to neighboring region) and signal-to-noise ratio (SNR: signal in the region of interest relative to background noise) is vitally important for specific visual guidance of tumor detection and removal. Sufficient CNR and SNR are achieved due to fluorophore accumulation in target tissue, while unbound fluorophore is rapidly moved from healthy tissues and clearance organs [11]. Nevertheless, most dyes are not tumor-specific and *in vivo* performance can be complicated by non-specific biological interaction, *e.g.* membranes, pharmacokinetic processes, including absorption, distribution, metabolism and excretion, and optical properties of the dye and tissue [12]. For instance, some cyanine-based NIRF probes with hydrophobic core structures and high surface charge bind to plasma proteins, which results in reticuloendothelial (RES) organ sequestration and hepatobiliary clearance *in vivo*, which can compromise tumor contrast [13–16]. Useful strategies for improving CNR and SNR include, among others, utilizing tumor or tumor microenvironment specific biomarkers [12] and altering excretion from the liver (hepatobiliary) to the kidneys (urinary) [17–19]. Pancreatic cancer CNR was found to be significantly increased by targeting somatostatin [20,21] or tumor cell antigens [22] or utilizing cell-penetrating peptides [23] for tumor-specific enhancement. Reported by Choi, *et al.* [15,16,24], improved tumor SNR was achieved by using zwitterionic fluorophores, which increased renal filtration and reduced overall background. Hence, we hypothesized that optimized pancreatic tumor contrast could be achieved by combining tumor-specific targeting and facilitating minimized intraperitoneal organ accumulation.

Previously, we reported the development of tumor-selective delivery of the FDA-approved NIR fluorophore, indocyanine green (ICG), by physically entrapping the dye in hyaluronic-acid (HA)-derived nanoformulations, termed NanoICG, in models of breast, prostate, and pancreatic cancer [25–28]. NanoICG resulted in significant pancreatic cancer

contrast relative to muscle reference and/or uninvolved pancreas, but also resulted in strong signal in intraperitoneal organs, especially the liver and spleen [28]. To maximize pancreatic ductal adenocarcinoma (PDAC) contrast enhancement and to minimize RES capture, we sought to specifically examine the role of HA molecular weight and NIRF dye properties. Compared to our previous study of using hydrophobically-modified HA to drive nanoparticle self-assembly and physicochemical entrapment of ICG [28], two dyes, Cy7.5 and IRDye800, were directly conjugated to HA of three different molecular weights ( $MW_N$ ), including 5, 20, and 100 kDa. The effects of HA  $MW_N$  and physiological properties of NIR dyes on tumor specificity and biodistribution were investigated to minimize RES uptake, reduce peritoneal organ background fluorescence, and determine a lead agent for PDAC enhancement with minimized RES uptake. These select agents would ideally be useful for detection of intraperitoneal metastatic pancreatic cancer or other tumor types that require surgical detection or intervention in the abdominal cavity.

## Results and Discussion

### Photochemical characterization of HA-dye conjugates

HA-Cy7.5 and HA-IRDye800 conjugates were synthesized with 1-Ethyl-3-(3-dimethylaminopropyl)-carbodiimide (EDC)/N-hydroxysuccinimide (NHS) coupling chemistry. The physicochemical and optical properties of HA-Cy7.5 and HA-IRDye800 are summarized in **Figure 1**, **Table S1**, and **Figure S1**. HA-Cy7.5 conjugates displayed distinct, solvent-dependent spectral properties: In  $H_2O$ , fluorescent peaks were quenched with broad absorbance spectra compared to dissociation in DMSO, indicating self-assembly and self-quenching, which is consistent with nanoformulation of Cy7.5 [29]. Cyanine dyes are capable of forming H-aggregates by hydrophobic interaction, which is characterized with hypsochromic absorption and weak fluorescence emission [30–32]. As shown in **Figure 1B** and **S1**, the absorption wavelength blue-shifted 80 nm for HA<sub>5k</sub>, HA<sub>20k</sub> conjugated Cy7.5, while a blue shift of only 10 nm was observed for HA<sub>100k</sub>-Cy7.5 conjugate in  $H_2O$ . Furthermore, upon disassembly in DMSO, the fluorescence emission intensity exhibited a red-shifted to 810 nm, and a 21.3-, 9.2- and 4.0- fold increase in fluorescence intensity for HA<sub>5k</sub>-, HA<sub>20k</sub>- and HA<sub>100k</sub>-dye conjugates, respectively. In comparison, hydrophilic IRDye800 displayed a limited tendency to interact with other IRDye800 molecules as opposed to interacting with

polar solvent (**Figure 1C**, **Figure S1**). The negative charge also prevents close interaction of the heterocyclic rings between dyes, compromising  $\pi$ - $\pi$  interaction. Therefore, conjugation of HA to IRDye800 had minimal impact on spectral properties of IRDye800 (**Figure 1C**).

It is worth noting that HA<sub>20k</sub>-dye conjugates are not nanoparticles (NPs) in aqueous phase. We examined the morphology and hydrodynamic diameter of HA<sub>20k</sub>-Cy7.5 with NP tracking analysis, dynamic light scattering, transmission electron microscopy and molecular docking, and concluded HA<sub>20k</sub>-Cy7.5 forms aggregates in the aqueous phase instead of self-assembled NPs (data not shown). BSA monomer is spherically shaped with a diameter of ~10

nm (**Figure S2A**). When mixed with HA<sub>20k</sub>-Cy7.5, BSA morphologically changed to irregular shape with sizes range from 10-70 nm (**Figure S2B**) and had elution time on size exclusion chromatography consistent with BSA (see **Figure 2**). In comparison, BSA monomer remains ~10 nm in the presence of HA<sub>20k</sub>-IRDye800. In summary, when conjugated with hydrophobic Cy7.5, HA-dye tends to aggregate and self-quench, but the fluorescence is recovered upon disassembly, or partially upon BSA interaction. No fluorescence quenching was observed with HA conjugated to the hydrophilic IRDye800, i.e., the spectral properties of HA-IRDye800 conjugates were conserved with or without BSA.

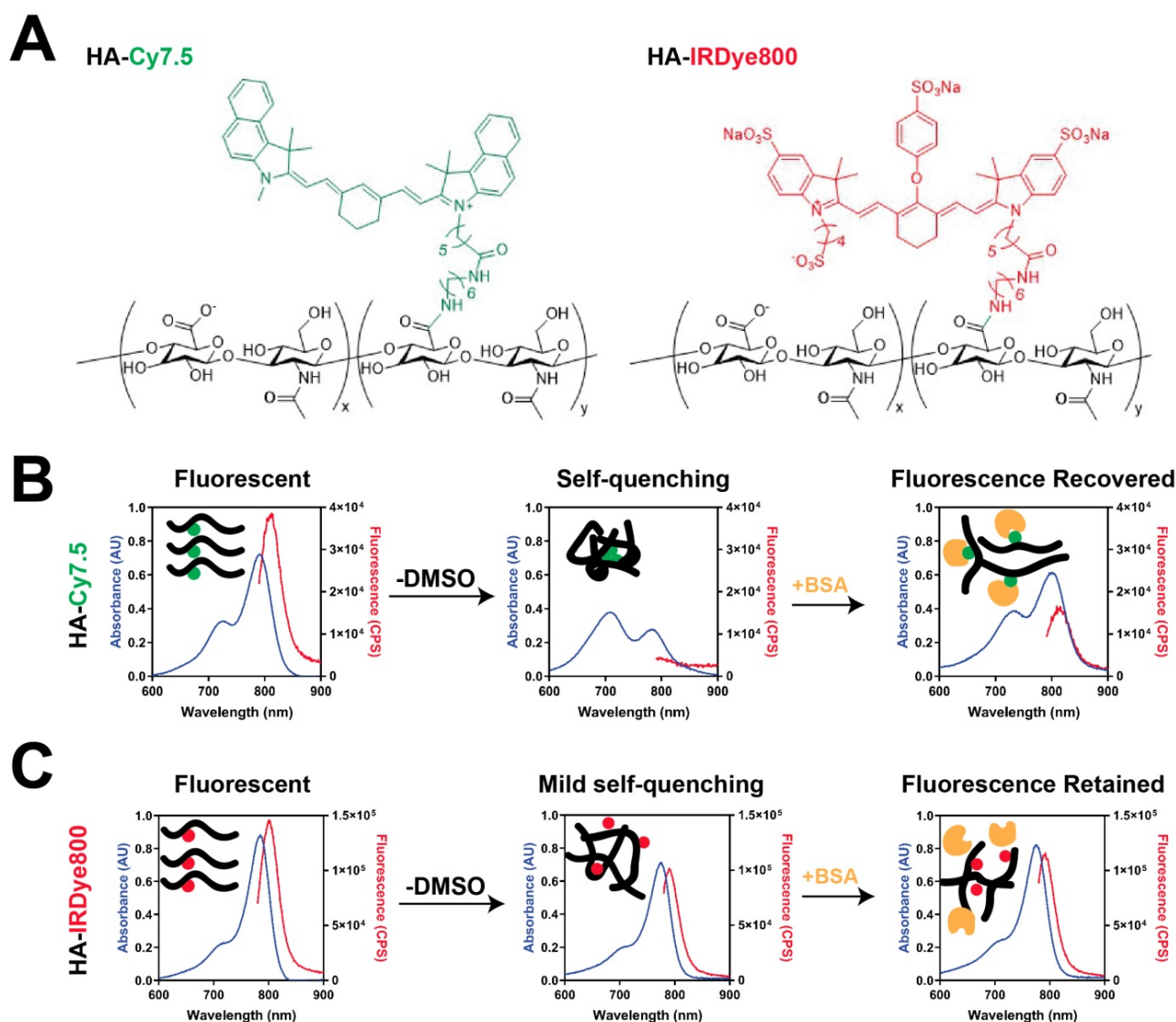


**Figure 1.** Characterization of HA-dyes with different HA MW<sub>N</sub>. **(A)** Chemical structures of HA-Cy7.5 and HA-IRDye800; x and y indicate the calculated number of disaccharide units and conjugated dyes per polymer chain, respectively; x = 9, y = 1 for HA<sub>5k</sub>-dye; x = 38, y = 1 for HA<sub>20k</sub>-dye; x = 169, y = 3 for HA<sub>100k</sub>-dye; **(B-C)** absorption and fluorescence emission pattern of HA-Cy7.5 and HA-IRDye800 in H<sub>2</sub>O, DMSO/H<sub>2</sub>O or BSA with corresponding schematic diagram of molecular interaction shown as insets; the absorption was collected between 600 nm to 900 nm, the fluorescence was excited at 775 nm for HA-Cy7.5 and 770 nm for HA-IRDye800, and collected between 790 nm to 900 nm for HA-Cy7.5 and 780 nm to 900 nm for HA-IRDye800. The concentration of free dye for HA-dye conjugates was consistent (4  $\mu$ M) among solutions with and without DMSO and in BSA.

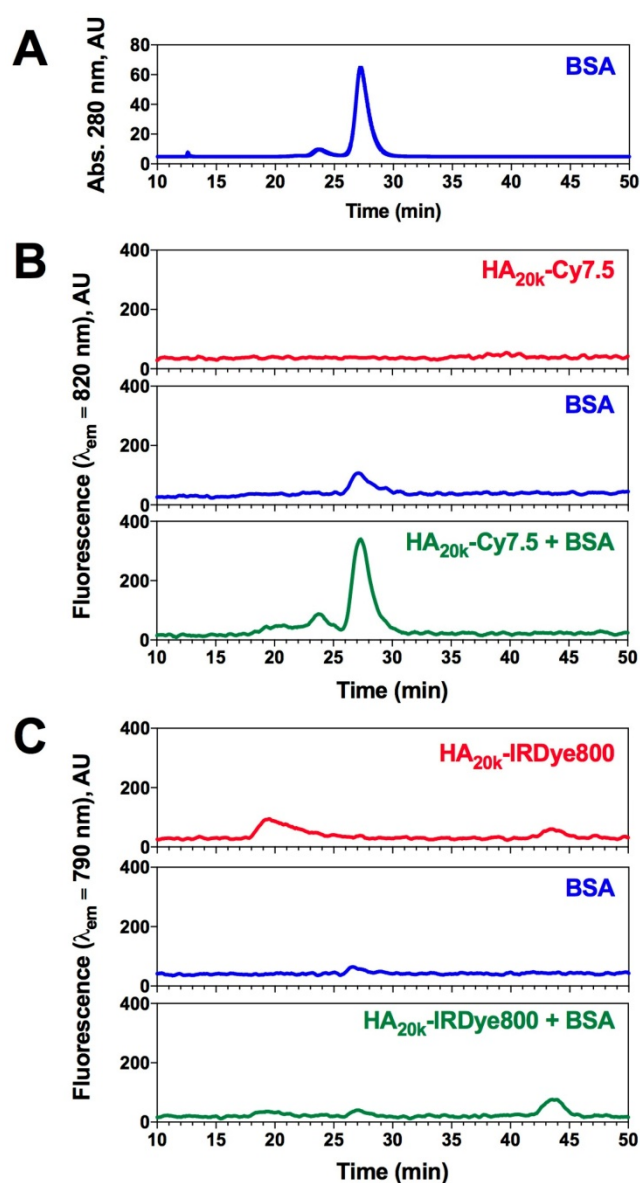


**Figure 2.** BSA has dye-selective interaction with HA-dye conjugates. (A) Elution chromatogram trace of 50  $\mu\text{M}$  BSA monitored at 280 nm absorption; (B) SEC chromatogram of HA<sub>20k</sub>-Cy7.5 (4  $\mu\text{M}$  Cy7.5 equivalent, red), BSA (50  $\mu\text{M}$ , blue) or the mixture (green);  $\lambda_{\text{ex}} = 775$  nm,  $\lambda_{\text{em}} = 820$  nm, integration (int) = 5 s; (C) SEC chromatogram of HA<sub>20k</sub>-IRDye800 (4  $\mu\text{M}$  IRDye800 equivalent, red), BSA (50  $\mu\text{M}$ , blue) or the mixture (green);  $\lambda_{\text{ex}} = 770$  nm,  $\lambda_{\text{em}} = 790$  nm, int = 5 s.

### Association of BSA with HA-dye conjugates

Plasma protein association can have a significant impact on *in vivo* size and solubility, which can alter pharmacokinetic properties and tissue specificity of systemically-administered agents [33]. To further investigate whether conjugated dye caused non-specific protein association, a mixture of HA-dye and BSA were separated for protein recognition while being monitored for NIRF to identify the presence of HA-dye. ICG+BSA was used as a control of known NIRF-protein interaction to calibrate the chromatography-spectrophotometric system. The delay volume between UV detector and

spectrofluorometer was  $5.55 \pm 0.18$  mL (determined by FITC labeled dextran2000 and ICG+BSA peaks) and normalized in Figure 2.

BSA monomer was eluted maximally at 27 min when monitoring absorbance at 280 nm (Figure 2A), whereas minimal signal was observed in NIRF channel at that time (Figure 2B-C, blue trace). The NIRF of HA<sub>20k</sub>-Cy7.5 was undetectable due to self-quenching (Figure 2B, red trace), whereas HA<sub>20k</sub>-IRDye800 exhibits 2 peaks which likely correspond to aggregate and dispersed polymer conjugate (Figure 2C, red trace). Interestingly, a NIRF peak was detected when HA<sub>20k</sub>-Cy7.5 was mixed with BSA at the elution time of BSA (Figure 2B, green trace), which was consistent with the fluorescence recovery displayed spectrofluorometrically (Figure 1B). A corresponding peak from HA-IRDye800 attributed to BSA binding was minimal (Figure 2C, green trace). In order to confirm the presence of BSA, fractionated eluate of interest from HA-dye + BSA were collected for Bradford assay, the NIRF peak fractions were strongly positive after Bradford dye staining, indicating that NIRF peak of HA-Cy7.5 corresponds to BSA elution (data not shown).

Berezin, *et al.* [34] demonstrated that the fluorophore, but not the targeting moiety, is predominantly responsible for albumin binding of imaging probes. Meanwhile, HA is capable of reducing protein adsorption and potentially the immunogenicity of the protein corona [35,36]. Cyanine dyes such as ICG, are able to bind with plasma proteins with high affinity, which results in complete extraction by hepatic paracyma and fast elimination into the bile [37,38]. More importantly, after examining several NIR fluorophores with structural similarity but varied number of hydrophilic groups, Berezin *et al.* found that more hydrophilic dyes exhibited up to 2 orders of magnitude lower binding constants toward albumin than their hydrophobic counterparts [34]. Cypate possess a stronger binding constant to albumin with a value of  $556000 \text{ M}^{-1}$ , whereas IRDye800 binds the weakest with a value of  $6100 \text{ M}^{-1}$  [34]. Though it is difficult to determine the non-covalent label's physico-chemical mechanisms (hydrophobic interactions, electrostatic interactions, and hydrogen bonding), structural modification to the aromatic moiety exhibited slight to moderate changes to the hydrophobic nature of the dyes. As a result, the BSA binding constant could be referred as a measure for hydrophilicity [39]. In addition, it is well-established that aromatic groups of the dyes primarily mediate albumin binding [40,41]. The accessibility of the dye's chromophore core to the conjugate system of BSA, which was affected by the length of sulfonate groups and conjugation, plays a

key role in albumin binding. As reported by Beckford, *et al.* [42], increased hydrophobicity of the indolium side chain results in enhanced binding interaction. In the specific case of Cy7.5 and IRDye800, the varied chromophore accessibility was the combined results of steric hindrance and electrostatic repulsion caused by the phenyl groups and sulfonate groups. Accordingly, our study demonstrated that HA-Cy7.5 displayed increased binding with BSA as compared to HA-IRDye800 (**Figure 2B-C**), which could be due to the benzoinole of Cy7.5 being more hydrophobic than the IRDye800 indole. Also, ionized sulfonate groups significantly decrease the hydrophobicity of IRDye800 and in turn decrease serum protein binding.

### Background Signal Interference can be Optimized to Detect Pancreatic Cancer

To investigate the hypothesis that protein association resulting from dye hydrophobicity/hydrophilicity and HA MW<sub>N</sub> could affect the biodistribution profile, each conjugate, or dye alone, was intravenously injected into wild type (WT) C57BL/6 mice or PDAC-bearing mice (age and gender matched), and then necropsied at either 24 or 96 h post injection. After necropsy, the fluorescence intensity was examined in each organ for both HA-Cy7.5, HA-IRDye800 and control groups. In the WT mice, the organs of interest, RES organs (liver, spleen and femur) and clearance organs (liver and kidney), were compared between different MW<sub>N</sub> of HA-dye for NIRF accumulation. HA-Cy7.5 conjugates primarily accumulated in liver, followed by spleen and kidney, among which, HA<sub>20k</sub>-Cy7.5 displayed the highest fluorescence intensity in liver that lasted for 4 days (**Figure S3A-B**, **Figure S2A**). As a comparison, HA-IRDye800 interacted slightly with albumin (**Figure 1C**, **2C**) and was able to retain the small size and hydrophilicity of HA and IRDye800. Therefore, the resulting biodistribution profile was attributed to the HA-IRDye800 conjugate rather than albumin (**Figure S3C-D**). When comparing different MW<sub>N</sub> of HA-IRDye800, HA<sub>5k</sub>-IRDye800 and HA<sub>20k</sub>-IRDye800 exhibited greater tendency to be accumulated and cleared in kidneys as compared to liver (**Figure S3C-D**, Video 2), whereas HA<sub>100k</sub>-IRDye800 appeared to be retained in RES organs.

The biodistribution pattern of non-pancreatic tissue was comparable between WT C57BL/6 mice (**Figure S3A**, **C**) and the PDAC mouse model (**Figure 3A-B**). In the PDAC-bearing mice, higher fluorescence signal was observed in pancreas from the HA-dye-administered group compared with the free dye group ( $p < 0.0001$ ). The fold-increase of NIRF signal of the pancreas was 8-28 for HA-Cy7.5 when compared to Cy7.5; and 8-15 for HA-IRDye800 when

compared with IRDye800 (**Figure 3A-B**).

Background organ interference ratios were quantified by dividing the fluorescent intensity of PDAC by that of visceral organs in the PDAC-bearing mice. These organs include muscle (reference tissue for non-NIRF accumulation), stomach, small intestine, liver, spleen and kidneys (surrounding organs or clearance organs). The ratios are summarized in **Table S2-3**. The ratio for PDAC: muscle was higher for HA-conjugated dye compared to the free dyes, and the ratio remained  $\geq 10$  after 96 h clearance (calculated from **Figure S4B**, **D**, **S5I**), thus presenting high PDAC specificity. The impact of clearance routes on tumor contrast was determined by quantifying the ratios of PDAC:clearance organs. The ratio for kidneys was 4.7 compared to 2.0 and for liver it was 0.5 compared to 1.8, for HA<sub>20k</sub>-Cy7.5 and HA<sub>20k</sub>-IRDye800 respectively (**Table S2**). The values indicate that the largest source of NIRF signal interference for the HA-Cy7.5 conjugates were the liver and spleen, while in HA-IRDye800 it was the kidneys.

An ideal molecular imaging agent should display suitable pharmacokinetics for visualizing the biochemical target/process of interest. Insights have been reported into the relationship between molecular structure and biologic behavior of cyanine dyes that's determined by the protein association [34,39,41,43,44]. Tian *et al.* [41] improved the pharmacokinetics with albumin-chaperoned cyanine dyes, the complex afforded impressive blood vessel resolution and expanded time window, when compared to free cyanine dyes. The dye-protein complexation strategy can be extended to antibodies for molecular targeted cancer imaging [41]. On the other hand, physiological parameters such as hepatic filtration, tissue extravasation, tissue diffusion, and kidney excretion are clearly impacted by imaging agent size, which has a profound impact on its *in vivo* distribution [45,46]. Often macromolecules (10 nm - 100 nm [45]) afford prolonged blood half-lives to allow time for extravasation out of the vasculature. Nevertheless, small particles exhibit lower background signal due to rapid clearance, but provided less time for the probe to access the tumor [47]. As a linear homopolymer, HA demonstrated MW-dependent-biodistribution [48]. Courel, *et al.* [49] found the retention of tritiated high MW (HMW)-HA was 40-fold higher than that of HA oligomers on nude mice 5 h post injection; in addition, the highest accumulation was in kidney for HA oligomers and in liver for HMW-HA. Though conjugated with NIR fluorophore, HA-IRDye800 demonstrated consistent MW-dependent biodistribution as HA (**Figure S3C-D**) because HA MW drives the *in vivo* fate instead of the hydrophilic fluorophore. The Cy7.5 moiety entropically favors

albumin binding (Figure 1B, 2B). Therefore, the increased size of the HA-Cy7.5 + albumin complex was excluded from renal filtration and entrapped and subsequently eliminated through hepatic filtration (Figure S3A-B).

### FIGS can Detect Pancreatic Adenocarcinoma

The representative FIGS images from HA-dyes displayed marked contrast between PDAC and healthy, uninvolved pancreas (Figure 4). Overall, HA-Cy7.5 exhibited higher fluorescence intensity than HA-IRDye800, including significant signal in the GI tract, especially for HA<sub>20k</sub>-Cy7.5. In comparison, HA-IRDye800 displayed comparable or greater contrast within the tumor-bearing pancreas along with negligible background signal from the GI tract. The fold increase of signal intensity when the excitation source is directed at the tumor compared to when the excitation source is directed off the tumor is 0.14 (Cy7.5), 2.10 (HA<sub>5k</sub>-Cy7.5), 3.59 (HA<sub>20k</sub>-Cy7.5), 9.17 (HA<sub>100k</sub>-Cy7.5), as detected at 825 nm, and 0 (IRDye800), 2.17 (HA<sub>5k</sub>-IRDye800), 663.09 (HA<sub>20k</sub>-IRDye800), 52.32 (HA<sub>100k</sub>-IRDye800), as

detected at 810 nm. The center of the directed excitation laser is indicated by green crosshairs. PDAC and UP were delineated with white dots. The PDAC specificity was maintained for up to 4 days post injection with HA-Cy7.5, but contrast was compromised over time for HA-IRDye800, especially for HA<sub>20k</sub> and HA<sub>100k</sub> (Figure S5) at 96 h.

The hand-held spectroscopic imaging device utilizes a NIR laser diode (emitting at 785 nm) coupled to a compact head unit for light excitation and collection. Its ability to resolve NIRF signals from background signal arises from the optical filtering that takes place in the hand-held pen. A dichroic mirror and a long pass filter attenuate Rayleigh scattering by a factor of  $10^8$  in the collection fiber, thus, only Stokes-shifted light is transmitted to the spectrometer [50]. The Spectropen is highly sensitive for measuring exogenous NIRF contrast agents during surgical procedures and it stably aligned and calibrated for robust surgical use, with the minimum spectrally-resolvable concentration of ICG at  $2.5 \times 10^{-11}$  M in the *in vitro* setting [50]. As compared to the imaging systems that relied on native fluorescence,

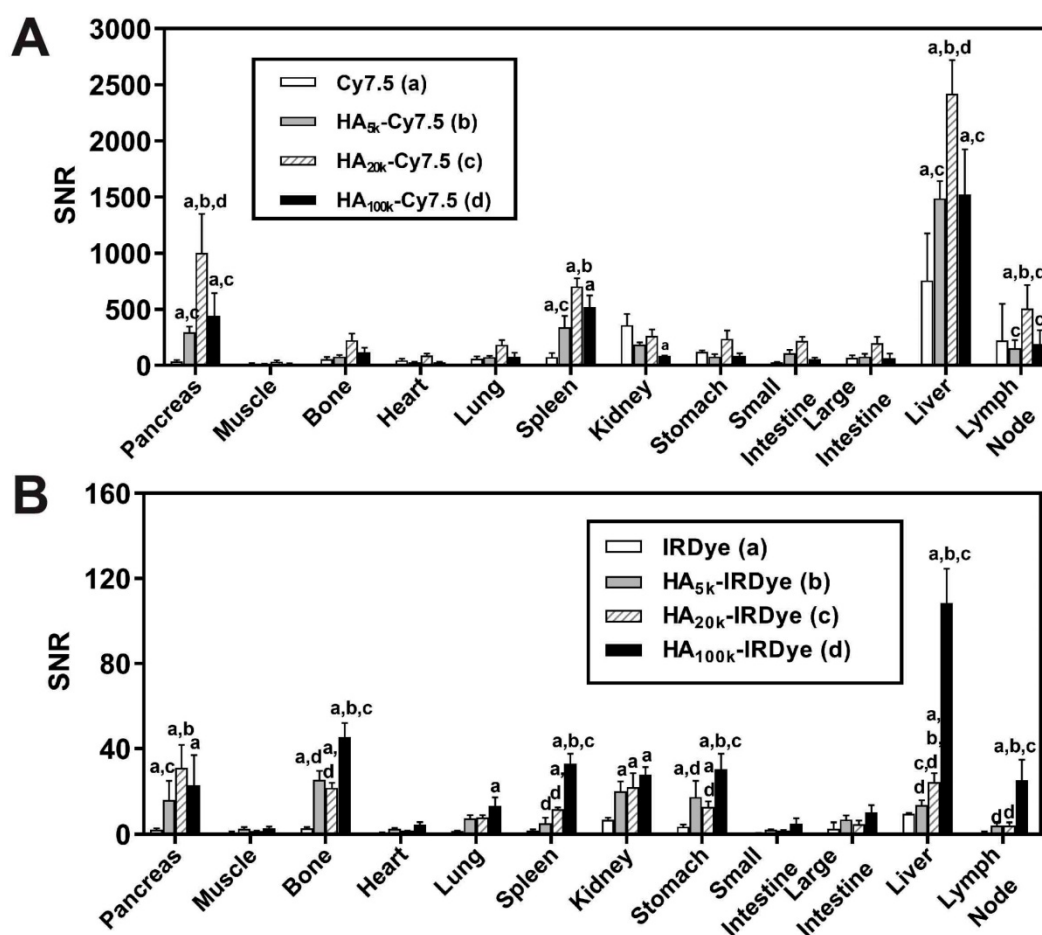


**Figure 3.** Quantification of biodistribution and the ratio of tumor contrast to accumulation/clearance organs from PDAC-bearing mice treated with HA-dye conjugates or controls 24 h post-administration. Relative organ biodistribution of (A) HA-Cy7.5 and (B) HA-IRDye800. Quantification was based on fluorescence intensity from NIRF images; N = 5, \**p* < 0.05 as compared to free dye, †*p* < 0.05 as compared to HA<sub>5k</sub>-dye, ‡*p* < 0.05 as compared to HA<sub>20k</sub>-dye, §*p* < 0.05 as compared to HA<sub>100k</sub>-dye.

incorporation of contrast agents into spectroscopic imaging also enables addressing the issue of tumor heterogeneity. In this study, the signal from UP in **Figure 4** might be interfered from intestinal tissue that is immediately beneath the UP. The UP signal could

also be the result of marginal distribution of the relatively brighter Cy7.5-based contrast agents. The signal in the heatmap is obtained solely from the excitation area of the laser, indicated by green crosshairs in **Figure 4**.

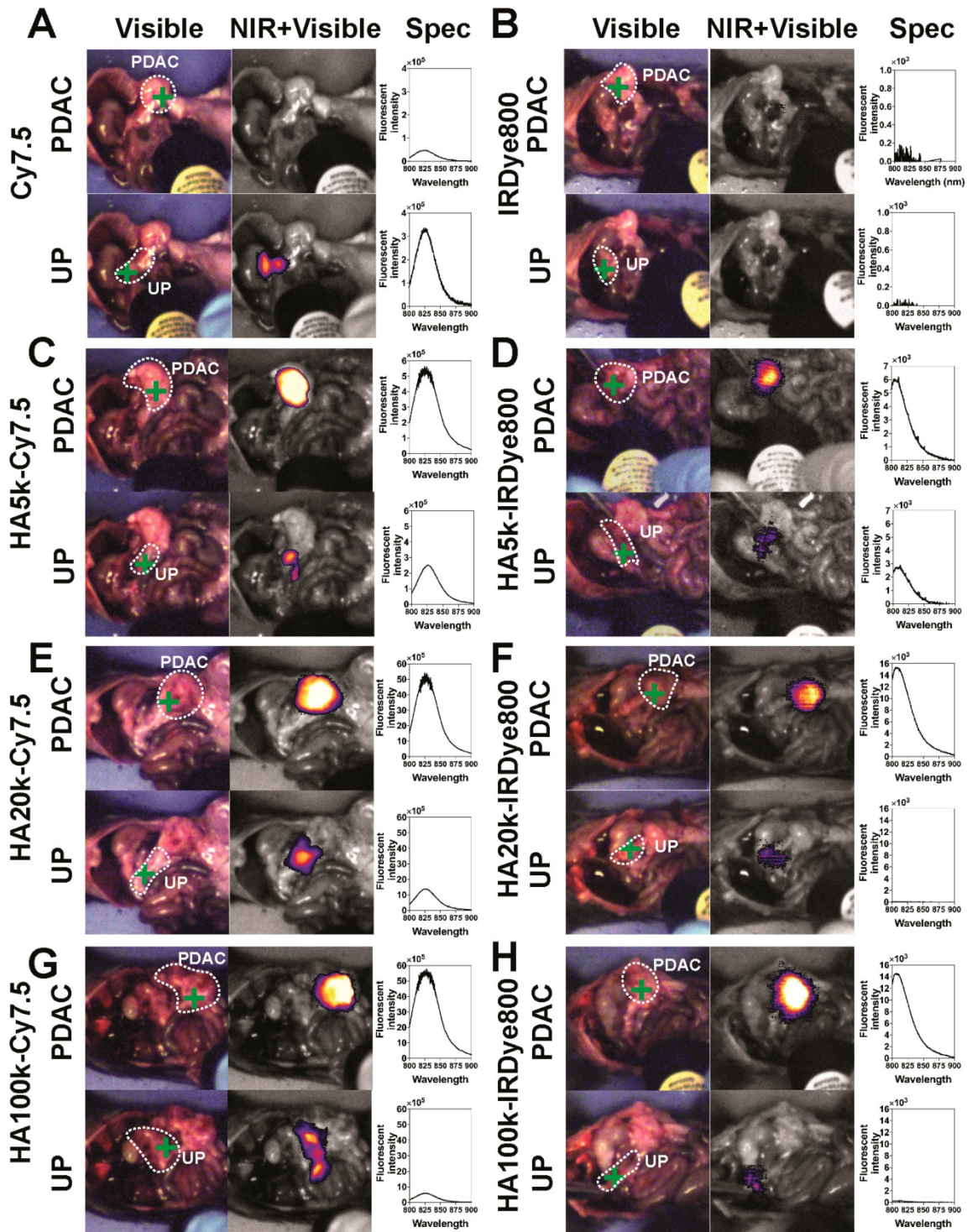


**Figure 4.** Images from optical surgical navigation of PDAC with contrast enhancement due to HA-dye or dye 24 h post *i.v.* injection. Livers and spleens were removed due to high background signal due to clearance, which interferes with pointed spectroscopic measurement. Spleens that were completely involved with PDAC were kept. Two channels (visible with/without NIR) and two spots [Spectropen directed at PDAC, uninvolved pancreas (UP)] were displayed for each experimental group; (Left) Color images depict orthotopic PDAC and the location of the handheld spectroscopic pen, which provides NIR spectral information and serves as an excitation source for a widefield imaging system; white dots outlined PDAC or UP. (Middle) NIR signal overlaid onto the grayscale image shows robust enhancement of syngeneic, orthotopic pancreatic cancer, green crosses indicate the directed location of excitation laser. (Right) Spectroscopic measurements quantifying the fluorescence intensity emitted from PDAC or UP. Improved contrast can be observed in HA conjugated dye groups. UP = uninvolved pancreas.

Tumor contrast enhancement relies not only on the accumulation of the contrast agent in tumor tissue, but also on the ability of the contrast agent to be cleared from healthy surrounding tissues and organs. Accumulation and clearance of imaging agent from tissue that is not malignant is the sum of several factors, including native dye clearance mechanism, physico-chemical properties of the contrast agent, and/or for potential phagocytic interaction, which directs agents to organs of RES [51,52]. Therefore, there are several important criteria that can be tuned to control the *in vivo* biodistribution of contrast agents [46]. Size and hydrophobicity are decisive factors for kidney elimination and RES sequestration [53]: generally, particles with a hydrodynamic diameter up to 5-7 nm fall below renal filtration threshold and are excreted [54], while particles larger than 200 nm can be trapped in liver and spleen with prolonged retention. Hydrophilicity variation affects the pharmacokinetics of the probes as a result of distinct protein adsorption, which is more likely for hydrophobic than hydrophilic materials [55]. Protein adsorption could mediate the enhanced RES sequestration by promoting opsonization [55]. More importantly, serum protein adsorption increases the apparent hydrodynamic diameter of a hydrophobic molecules by more than 15 nm, which prevents renal excretion [19]. The optimum pharmacological properties for *in vivo* application include minimum non-specific binding and an adequate retention time in the body preferably followed by fast excretion [56]. A better understanding with regard to how the characteristics of contrast agents influence their *in vivo* behavior is an important step towards designing NIRF biomaterials suitable for molecular imaging applications and for efficient tumor delivery [52].

### Ex Vivo Analyses of NIRF Contrast in PDAC-bearing Pancreata

As observed in **Figure 5** and **Figure S6**, NIRF images (*Top row*) of the pancreas indicated that HA<sub>20k</sub>-NIRF conjugates did not accumulate in the healthy pancreas (HP) of WT mice (**Figure S6**), or uninvolved pancreas (UP) of PDAC tumor-bearing mice (**Figure 5A-B**), but accumulated in the PDAC portion of the pancreas, thus indicating an enhanced PDAC specificity. Additionally, HA<sub>5k</sub>- and HA<sub>100k</sub>-NIRF conjugates also specifically-accumulated in the pancreatic tumor, but with lower intensity than HA<sub>20k</sub>-NIRF conjugates. The NIRF intensity from the Spectropen at acquisition locations across the pancreas is consistent with the NIRF intensity profiles of the tumor-bearing pancreata imaged with LI-COR

imaging system (**Figure 5A-B**). A board-certified pathologist (GAT) identified tumor with histopathology and areas with high NIRF signal were also areas identified as poorly differentiated PDAC (**Figure 5A-B**), which is well-perfused by HA<sub>20k</sub>-NIRF as compared with HA<sub>5k</sub>-NIRF and HA<sub>100k</sub>-NIRF. Signal was not detected in free dye-treated PDAC or healthy pancreas. Contrast was still visible after 4 days of clearance (**Figure S7**), especially for the 100k HA conjugates. In summary, HA conjugated dyes are effective at the specific identification of PDAC, with HA<sub>20</sub> being the most efficient vehicle for PDAC delivery.

To investigate the relationship between potential HA-CD44 targeting and PDAC contrast-enhancement, both KPC (LSL-Kras<sup>G12D/+</sup>; LSL-Trp53<sup>R172H/+</sup>; Pdx-1Cre) mice-derived PDAC cells and resected tumor specimens were analyzed for CD44 expression (**Figure S8**). Additionally, single-stained flow cytometry (FC) histogram demonstrates that KPC cells were positive for CD44, (**Figure S8A**) with a stain index of 12.45 AU compared to 2.94 AU or primary pancreatic epithelial (PPE) cells (Quantified from FC). The necropsied tumors were composed of markedly atypical, non-cohesive epithelioid cells with marked nuclear pleomorphism and numerous mitotic figures. In some areas, the tumor cells demonstrated a spindle cell morphology suggestive of sarcomatoid differentiation. CD44 staining revealed strong, diffuse membrane staining in all tumor cells with both appearances (**Figure S8B**).

To compare the contrast enhancement of HA-dye statistically and quantitatively, SNR of PDAC was divided by that of uninvolved pancreas or healthy pancreas from WT mice. As shown in **Figure 5C**, no significant difference of NIRF signal was detected between uninvolved pancreas and healthy pancreas, regardless of contrast agent treatment. In comparison, a significantly-higher signal was detected between PDAC and uninvolved pancreas for HA<sub>5k</sub>-, HA<sub>20k</sub>- and HA<sub>100k</sub>-Cy7.5, HA<sub>5k</sub>- and HA<sub>20k</sub>-IRDye800 but not HA<sub>100k</sub>-IRDye800 treated mice, the contrast ratio (defined by SNR of PDAC/SNR of UP) was labeled in each figure. HA<sub>20k</sub>-IRDye800 displayed the highest fold-increase of 14.0, with  $p < 0.001$ . HA-Cy7.5 exhibited increased contrast as compared to Cy7.5, regardless of MW<sub>N</sub> of HA. Furthermore, enhanced contrast within PDAC pancreas was detectable after 4 days, with a contrast ratio of 3.86 and 5.96 for HA<sub>20k</sub>-Cy7.5 and HA<sub>20k</sub>-IRDye800, respectively (**Figure S7I**).

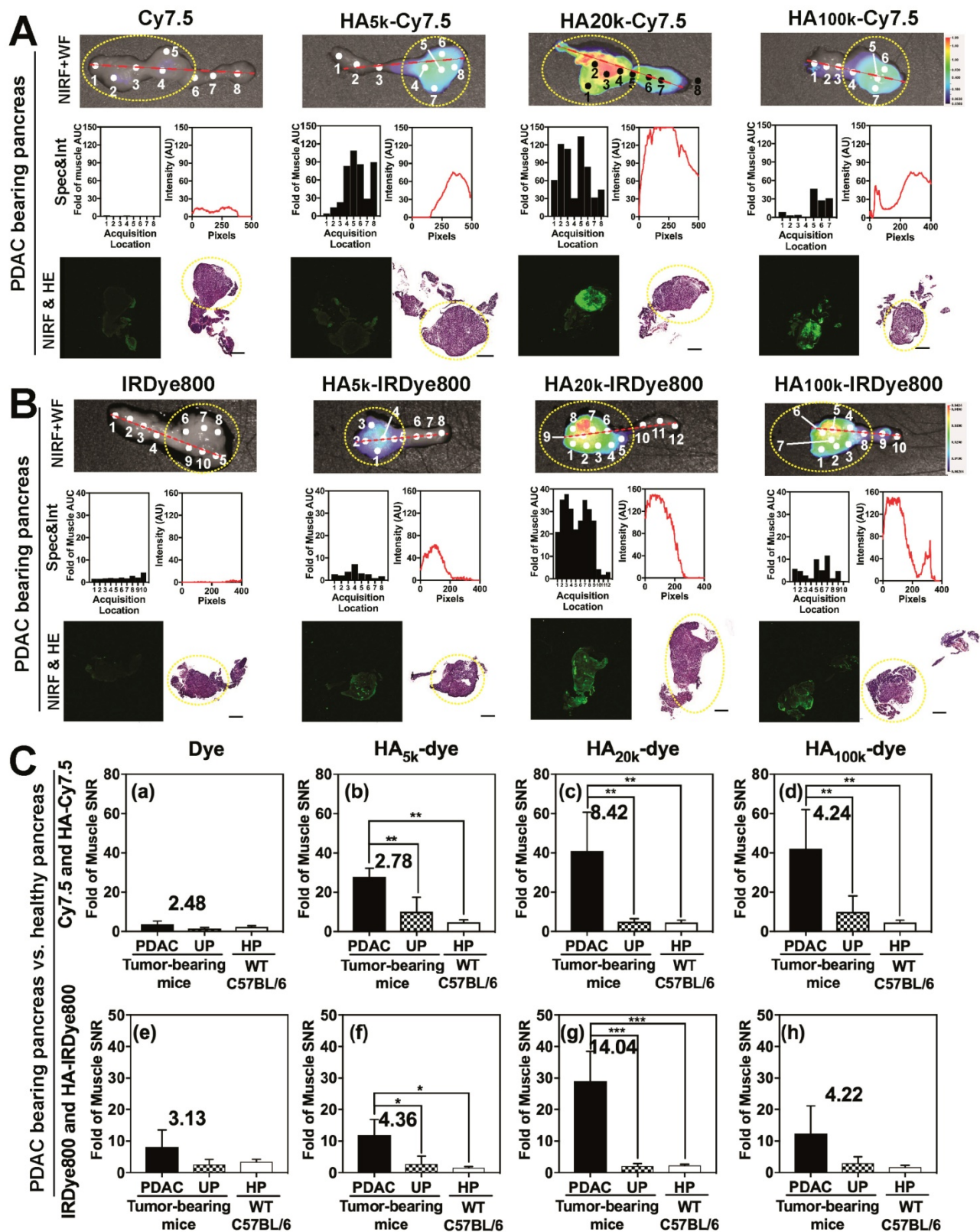


**Figure 5.** Ex vivo analysis of HA-dye accumulation within the pancreases from tumor-bearing mice. Panel **A-B** were arranged into three rows for each group: (Top) NIRF and white-field (WF) images of a representative PDAC-bearing pancreas marked with acquisition locations of the spectroscopic signal shown in middle row. Yellow dashed lines circle indicated the PDAC portion of pancreas.; (middle, left) fluorescence intensity excited with 80 mW laser power and 1 s integration time with the excitation laser component of FIGS system; (middle, right) plots of intensity values along the red dashed line from the NIRF images quantified by ImageJ; (bottom, left) scanned image of frozen-sectioned unstained healthy/PDAC-bearing pancreas with NIR channel from Odyssey Clx imaging system; (bottom, right) scanned H&E stained pancreas slides with Panoramic 250 flash series digital scanner, for each group pancreases were sequentially sectioned with unstained slides. Yellow dashed lines circle indicated the PDAC portion of pancreas. All scale bars represent 2 mm; (C) SNR of PDAC, uninvolved pancreas (UP) and healthy pancreas (HP) normalized by muscle SNR that's been treated with (a) Cy7.5, (b) HA<sub>5k</sub>-Cy7.5, (c) HA<sub>20k</sub>-Cy7.5, (d) HA<sub>100k</sub>-Cy7.5, (e) IRDye800, (f) HA<sub>5k</sub>-IRDye800, (g) HA<sub>20k</sub>-IRDye800, (h) HA<sub>100k</sub>-IRDye800. Contrast data was obtained 24 h after i.v. injection. SNR values were calculated from NIRF images obtained with the Pearl Trilogy Small Animal Imaging System. \*\*\**p* < 0.001, \*\**p* < 0.01, \**p* < 0.05, N = 4-5 for each group.

The tumoral retention of HA-dye depends on the interstitial binding of HA moiety after blood circulation and extravasation. PDAC is hypovascular with collapsed, but intact blood vessels, which is not desirable for EPR effect [57–59]. Cabral, *et al.* [60] reported that sub-30 nm micelles could penetrate vasculature of pancreatic tumor. The calculated experimental hydrodynamic diameter of 30 kDa HA is 15 nm, while 32 nm for 100 kDa HA [61]. Therefore, HA<sub>5k</sub>, HA<sub>20k</sub> conjugated dye are presumed to extravasate more easily than HA<sub>100k</sub>-dyes, meanwhile vascular bursts could potentially enhance permeability of pancreatic tumor blood vessels for large particles [62]. Additionally, PDAC is characterized with an extensive extracellular HA deposition, which is (34 ± 2.7) ng/mg tissue for normal pancreas in contrast to (420 ± 150) ng/mg for PDAC in KPC mice [63–65]. A wide variety of HA binding molecules (serum-derived HA-binding protein, versican) and receptors (CD44, LYVE-1, RHAMM) contribute to the formation of HA meshwork and anchorage to the cell surface [64]. Followed with extravasation, HA moiety of contrast agents bind to overexpressed CD44 (or potentially other HA binding receptors) (Figure S8), which could confine the conjugates in tumor interstitium as opposed to diffusing back into blood vessels. Furthermore, the binding affinity relates with HA MW:HA oligomers with size of 38 disaccharide units (around HA<sub>20k</sub>) showed higher avidity with CD44 compared with that of 10 disaccharide units (around HA<sub>5k</sub>) due to multivalent binding [66]. In summary, PDAC vasculature is available for LMW HA-dye's extravasation, and HA-CD44 binding plays a role in retention within tumor, which may be the mechanism of HA-dye's robust contrast in PDAC.

### Contrast Enhancement for the Detection of Primary PDAC and Intraoperative Metastases with Widefield Imaging

We further investigated the role of RES accumulation (HA<sub>20k</sub>-Cy7.5) and kidney accumulation/elimination (HA<sub>20k</sub>-IRDye800) in contributing to the PDAC contrast by employing widefield imaging systems to simultaneously capture the NIRF distribution among organs of interest (Figure 6, Video 1-3). Overall both conjugates preferentially accumulate primary PDAC (Figure 6A, 6C, organs labeled 6+7), and more interestingly, intraoperative metastatic lesions (Figure 6A, 6C organ labeled 8) with high contrast. HA<sub>20k</sub>-Cy7.5 (Figure 5A-B) exhibited significant accumulation in liver and spleen as compared to HA<sub>20k</sub>-IRDye800 (Figure 5C-D), even with one tenth of the dose of dye as compared to HA<sub>20k</sub>-IRDye800. The NIRF signal is

evident in liver and small intestines as compared to the kidneys due for HA<sub>20k</sub>-Cy7.5 (Figure 5A-B). On the other hand, HA<sub>20k</sub>-IRDye800 (Figure 5C-D) is clearly observed in the kidneys, ureters, and bladder, which supports renal elimination of small, hydrophilic HA-conjugates.

Because Cy7.5 is brighter than IRDye800 [67] (also demonstrated in the different SNR scaling of axes in Figure 3), when injected with the same doses of HA<sub>20k</sub>-NIRF (equivalent to free dye), NIRF signals from HA-Cy7.5 conjugates were saturated on the Lab-FLARE® imaging system, while not detectable for IRDye800-based conjugates. In order to compare the relative organ accumulation between the two contrast agents while keeping the imaging parameters consistent, we adjusted the injection doses of HA<sub>20k</sub>-IRDye800 to 10 nmol of IRDye800 per mouse. We also determined the acute systemic toxicity with the adjusted doses and did not observe HA<sub>20k</sub>-IRDye800 induced toxicity, as shown in Figures S9-S10.

Handheld NIR spectrometers have been used for the quantitative analysis of solid pharmaceutical formulation [68]. Judy *et al.* [69] compared digital imaging with spectroscopy in quantifying fluorescent signal-to-background ratios *in vitro*, murine xenografts, tissue phantoms and clinically, concluding that spectroscopy was the most sensitive in identifying small numbers of cells, and tumors in deep tissue. Even though spectroscopic imaging has superior resolution than digital imaging, it suffers from a limited field of view and was time-consuming for data processing. While digital imaging was the most practical considering its wide field of view, background noise filtering capability and sensitivity to increasing depth, making it useful for broad exploration of the wound and body cavity. The detection threshold of ICG for digital imaging is 10 times higher than that of spectroscopy. In present study, the dose of IRDye800 for whole body fluorescence imaging was 10 times higher than that of Spectropen to achieve comparable signal and contrast, demonstrating lower sensitivity of fluorescence with whole-body fluorescence imaging. Considering the pros and cons for each imaging instrumentation, a useful strategy would be to use digital imaging to scan large regions of body cavity and the wound, and to use spectroscopic device for more detailed analysis of margins and micrometastases.

HA<sub>20k</sub>-NIRF conjugates were able to identify abdominal lesions smaller than 7 mm<sup>3</sup> and lymphatic metastases (Figure 7, Video 3). The presence of malignant tissue was supported by the hematoxylin and eosin (H&E) and positive staining of Ki-67 (Figure 7B-C). To that end, detailed histopathology

investigation confirmed contrast enhancement of several primary and metastatic PDAC malignancies. Sections of the primary lesion demonstrate nodules of epithelioid tumor cells within a peri-pancreatic lymph node and fat, the latter associated with a prominent inflammatory response (**Figure 7B**). The tumor cells demonstrated marked cytologic atypia without definitive glandular formation and adjacent pancreatic parenchyma was unremarkable. Immunostaining revealed that the tumor cells showed strong, diffuse membranous staining for CD44 in the background of expected staining within lymphocytes. While Ki-67 labeled >90% of tumor nuclei. PDAC invasion into soft tissue immediately adjacent to the pancreas had some areas that were more poorly

differentiated with foci having a sarcomatoid appearance (**Figure 7C-a**). CD44 stained all tumor cells and Ki-67 labeled approximately 75% of all tumor nuclei. PDAC metastases to adipocytic tissue (**Figure 7C-c**) had consistent morphology and showed diffuse CD44 and strong cytoplasmic staining. Ki-67 labels 50-60% of tumor nuclei. In **Figure 7C-d**, tumor cells are seen involving adipose tissue, surrounding individual adipocytes. Interestingly, there is heterogeneity of morphology with some tumor cells being epithelioid with others having a spindled, sarcomatoid appearance. CD44 strongly labels all tumor cells, which could play a role in HA targeting of these malignancies.

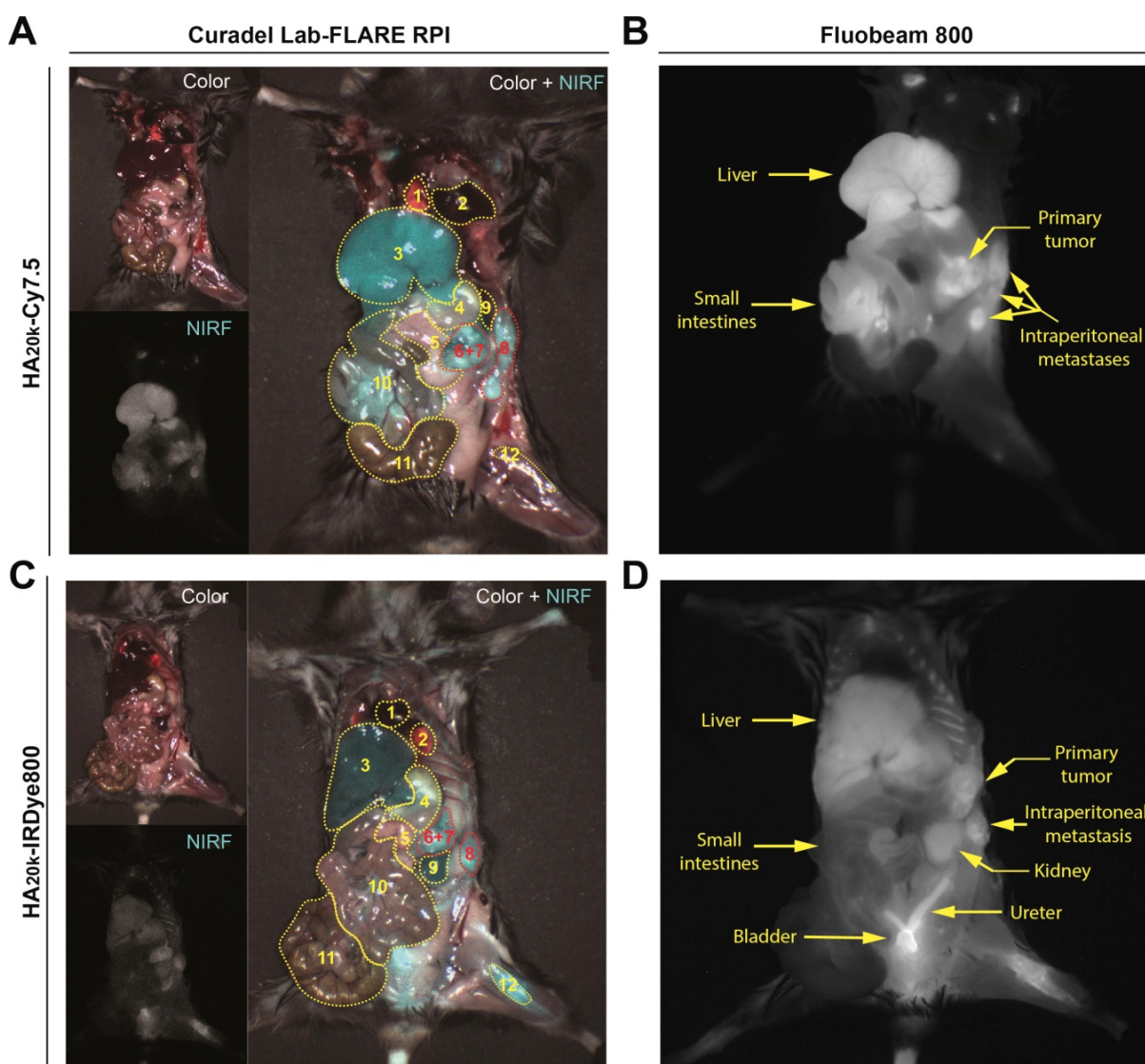


**Figure 6.** Representative whole-body images of PDAC-bearing mice captured by the Lab-FLARE RPI (A, C) or Fluobeam 800 (B, D) imaging system 24 h post injection of contrast agents. Images were captured from the color and NIRF channel and merge channels of the Lab-FLARE RPI imaging system are shown on the left, while images obtained by the Fluobeam 800 imaging system are shown on the right. The administered dose was 1 nmol of Cy7.5/mouse for HA<sub>20k</sub>-Cy7.5, and 10 nmol IRDye800/mouse for HA<sub>20k</sub>-IRDye800. 1- Heart, 2- Lung, 3- Liver, 4- Stomach, 5- Uninvolved pancreas, 6+7- Primary pancreatic tumor and involved spleen, 8- Intraperitoneal tumor, 9- Kidney, 10- Small intestines, 11- Large intestines, 12- Femur. Yellow dotted lines indicate the organs of interest and are labeled at the bottom of the figure. The intensity (cyan pseudocolor; Curadel Lab-FLARE RPI) and (grayscale colormap; Fluobeam 800) represents the NIRF accumulation. *N* = 3.

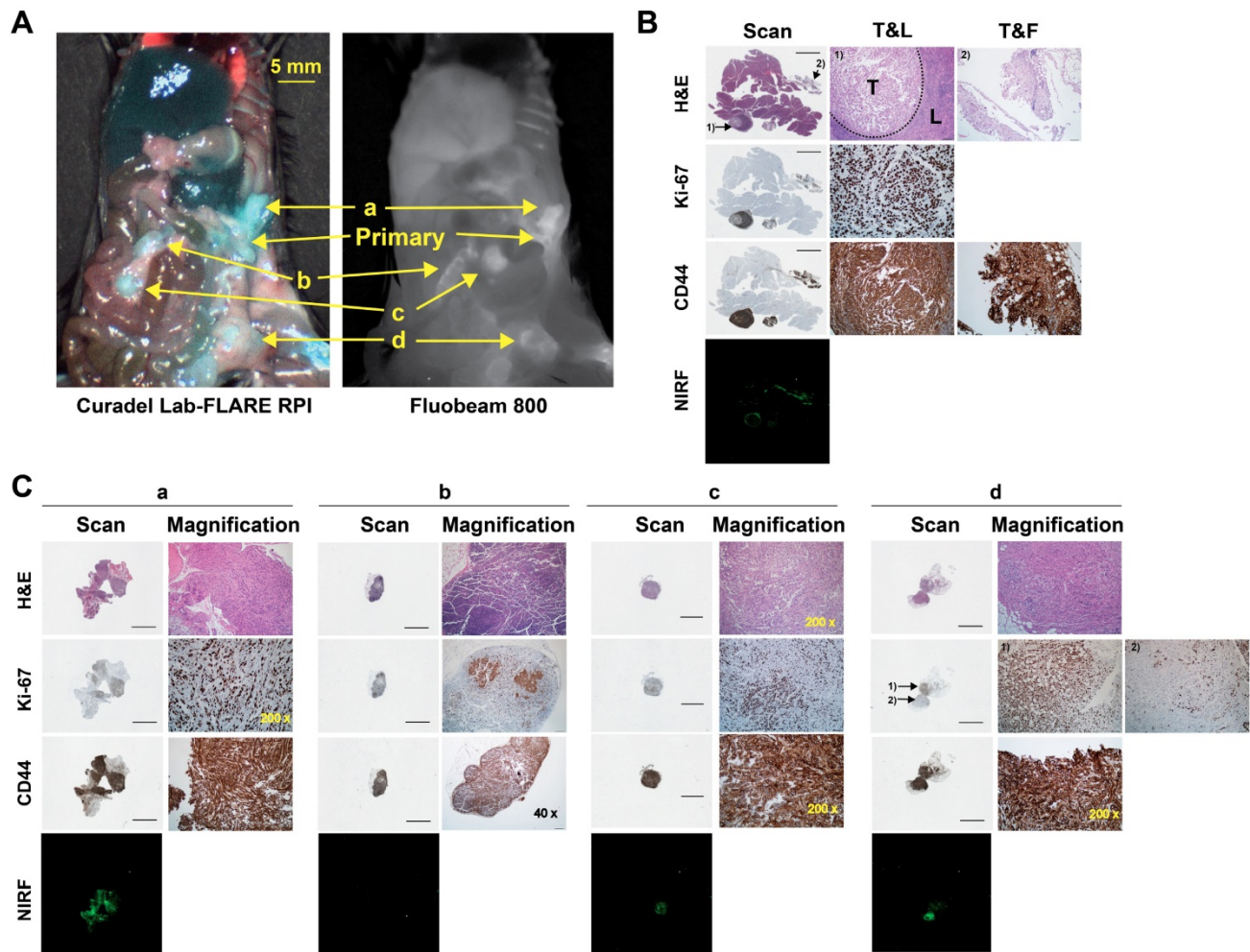


**Figure 7.** Probing capability of HA<sub>20k</sub>-IRDye800 on the intraperitoneal metastases of PDAC-bearing mice. **(A)** Fluorescence was accumulated at the metastatic sites of interest confirmed by the two wide-field imaging systems; a, b, c, d pointed at the suspected sites of metastases. **(B)** Pathology of primary tumor that was involved with spleen identified with H&E, Ki-67, and CD44 staining, NIRF distribution of corresponding sectioned was determined with 42  $\mu$ m resolution. The intensity of 800 nm channel of Odyssey Clx imaging system was set at 9. Black bars represent 2 mm on the scanned images. T&L refers to tumor and lymphatic tissue, T&F refers to tumor and fat. 1) and 2) are 200  $\times$  magnification of the site pointed at the scanned images. **(C)** Scanned and magnified images with power labeled at right corner. 1) and 2) in d refers to the well differentiated and poorly differentiated tumor, respectively.

Up-regulation of CD44 correlated with distant metastases and aggressive malignant behaviors of pancreatic cancer [70–72]. The regulation of tumorigenesis and cancer metastasis by CD44 was reported to be partially *via* PI3K/AKT or MAPK/ERK regulatory pathway [72]. Specifically, PDAC cells expressing high levels of CD44s with a mesenchymal-like phenotype were highly invasive and developed gemcitabine resistance *in vivo* [70]. CD44 is also reported to be a cancer stem cell marker for pancreatic cancer cells [73,74]. In clinical setting, CD44 expression could help identify patients at high risk of early recurrence and provide diagnostic value for more aggressive treatment after radical surgery [75]. Hence, targeting CD44<sup>high</sup>-expressing cells may provide diagnostic/therapeutic strategy for improving survival. In this study, we use CD44 as the malignant biomarker, which has been confirmed to be specifically and over-expressed in the tumoral

cells/samples (Figure S8). Though Ki67 is not a specific marker for PDAC, while subculturing KPC-derived cancer cells, we found the population doubling time is less than 24 h, which is in accordance with Torres *et al.*'s finding that doubling time of KPC-derived cells could be as short as 33 h, as compared with Pan02 (56 h) and AsPC-1 (58 h) [76,77]. On the contrary, the primary pancreatic epithelial cells from C57BL/6 mouse have the doubling time around 1.5–2.5 days. Due to the relatively high proliferative efficiency, Ki67 was used to differentiate KPC cells from benign cells as well.

## Conclusion

The results of this study demonstrate that contrast agent biodistribution can be controlled to specific clearance organs while maintaining strong tumor CNR. In particular, SNR was tuned to minimize the signal from liver, spleen, and GI tract.

Overall, HA-dye conjugates provide a straight-forward, but versatile platform to intraoperatively image pancreatic cancer. The strategy to reroute the native clearance of cyanine dyes from hepatobiliary to renal elimination and ease the RES burden of macromolecules results in the finding of optimized contrast agent (HA<sub>20k</sub>-IRDye800) with minimal non-specific accumulation in background organs. For conjugates using IRDye800, the dominant factor was HA MW. As shown with the HA-Cy7.5 conjugates, protein association with Cy7.5 normalizes biodistribution to the RES regardless of HA MW. On the contrary, LMW HA-IRDye800 conjugates (5 and 20 kDa HA) are likely below the renal threshold resulting in reduced RES accumulation. This is due in part to the HA MW, but also the lower propensity of IRDye800 to bind serum proteins compared to Cy7.5, as even HA<sub>5k</sub>-Cy7.5 is rerouted to RES accumulation and/or hepatobiliary circulation. Consequently, further detailed studies are ongoing to evaluate specific protein bound populations with these conjugates, pharmacokinetic profiles, and long-term biodistribution and clearance profiles of the lead HA conjugates. The rationale approach reported here control biodistribution could be applied to other delivery systems to minimize RES organ toxicity of therapeutic agents. Alternatively, directing imaging agents away from the kidney would benefit those with renal failure, where administration of certain renally clearing probes is contraindicated.

## Methods

*Materials and Reagents:* Cy7.5 amine was purchased from Lumiprobe (Hallandale Beach, FL); IRDye800CW trifluoroethylamine was purchased from LI-COR (Lincoln, NE); 5 kDa, 20-30 kDa, and 100 kDa sodium hyaluronate were purchased from Lifecore Biomedical (Chaska, MN). Lyophilized powder of BSA was purchased from Sigma (St Louis, MO). Sephadex G-25 PD-10 desalting column was purchased from GE Healthcare (Pittsburgh, PA); KPC cells were obtained from the diseased pancreas of KPC mice which were shared by Dr. Hollingsworth. 10-week-old female C57BL/6J mice were purchased from Jackson Laboratories (Bar Harbor, ME). 5.0 chromic gut and 5.0 nylon surgical sutures were purchased from Johnson & Johnson (Somerville, NJ). FITC-labeled CD44 antibody, purified rat mouse BD Fc blocker, propidium iodide (PI) staining solution and FC staining buffer was purchased from BD Bioscience (San Jose, CA). All other chemicals were purchased from Fisher Scientific and used at analytical grade.

*Conjugation and characterization of Cy7.5 or IRDye800 HA Conjugates:* Sodium hyaluronate (3.3-6.9

mg, MW<sub>N</sub> = 5 kDa; 9.5-10.7 mg, MW<sub>N</sub> =20-30 kDa; 10.2-12.7 mg, MW<sub>N</sub> =100 kDa) was completely dissolved in 2 mL of water. EDC and NHS (both 10× molar ratio to amine group), were then dissolved in the HA solution. After 15 min of activation, the pH was raised to 7.2, and Cy7.5-NH<sub>2</sub> (dissolved in DMSO) or IRDye800-NH<sub>2</sub> (dissolved in ultrapure water) –at 3× molar ratio to disaccharide unit per HA<sub>5k</sub> and HA<sub>20k</sub> chain and 9× for HA<sub>100k</sub> chain – was each added dropwise to each of the activated HA solutions under constant stirring. The reaction was allowed to proceed for 24 h at room temperature (rt). The reaction contents were then transferred to dialysis tubing (MWCO = 3500 Da for HA<sub>20k</sub>- and HA<sub>100k</sub>-dye conjugates; MWCO = 1000 Da for HA<sub>5k</sub>-dye conjugates, Spectrum Laboratories, Rancho Dominguez, CA). HA-Cy7.5 conjugates were dialyzed against 1:1 EtOH:H<sub>2</sub>O for 24 h followed by H<sub>2</sub>O for an additional 48 h. HA-IRDye800 conjugates were dialyzed against H<sub>2</sub>O for 24 h. The HA-dye conjugates were removed from the dialysis tubing, purified by PD-10 column, lyophilized, and stored at –20 °C. Dye content of HA-dye conjugates was determined relative to dye solutions using absorbance and fluorescence spectroscopy. Specifically, an Evolution 220 spectrophotometer (Thermo Fisher Scientific, Madison, WI) was used for scanning absorbance spectra (600-900 nm) and a FluoroMax-4 spectrofluorometer (Horiba, Edison, NJ) was used for quantifying fluorescent intensity of dye, HA-dye, disassembled and BSA-associated HA-dye from 770 to 900 nm. BSA solution was prepared at 0.33 mg/mL (5 μM) and HA-dye conjugates were prepared at 4 μM of free dye for **Figure 1B-C** and **Figure S2-3**. FEI Tecnai G2 Spirit transmission electron microscope (Hillsboro, OR) equipped with AMT digital imaging system were employed for TEM imaging.

*Determination of nonspecific serum protein binding:* BSA (50 μM, Sigma-Aldrich, MO) was incubated with HA<sub>20k</sub>-Cy7.5/IRDye800 (4 μM dye equivalent) in phosphate buffer (0.01 M, pH 7.4) for 1 h at rt. 1 mL of mixture or corresponding control (HA-dye conjugate only or BSA only) was filtered through 0.22 μm filter (Fisher Scientific, Hampton, NH) before loading onto an AKTA Pure 25 L Chromatography system (GE Healthcare, Sweden) that was equipped with Superdex200 Increase 10/300 GL column, UV monitor (fixed wavelength at 280 nm), and a fraction collector. For kinetic fluorescence measurements, an outlet portal was connected to a micro cuvette (Starna, Atascadero, CA) for monitoring the fluorescence of the eluent using the fluorescence spectrophotometer. Sample was eluted at flow rate of 0.45 ml/min for 60 min. Kinetic monitoring of fluorescence was collected for 66.7 min with 5 s integration time for HA<sub>20k</sub>-Cy7.5

(slit width was 20 nm,  $\lambda_{\text{ex}} = 775$  nm,  $\lambda_{\text{em}} = 820$  nm) and HA<sub>20k</sub>-IRDye800 (slit width was 10 nm,  $\lambda_{\text{ex}} = 770$  nm,  $\lambda_{\text{em}} = 790$  nm).

**Tumor model induction:** All animal studies were performed under a protocol approved by the UNMC Institutional Animal Care and Use Committee. Procedures were followed in accordance with institutional guidelines per the Guidelines on the Care and Use of Animals for Scientific Purposes to ensure humane care of the animals. Orthotopic, syngeneic PDAC induction was performed as described in previous studies [28,78]. Briefly, mature female C57BL/6 mice were selected for orthotopic tumor challenge using 10,000 KPC cells per mouse. Once anesthetized, a ~5 mm incision was made into the skin and peritoneum on the abdomen between the hip and rib. This allowed for the spleen to be exteriorized for injection of PBS cell suspension into the body of the pancreas. The peritoneum and skin were then secured using an internal dissolving chromic gut and a 5.0 nylon surgical suture, respectively. Animals were warmed, hydrated, and monitored until consciousness was regained. Within two weeks of introduction of tumor cells, palpable tumors were detected in all challenged mice.

**Biodistribution of HA-Dye conjugates as measured by fluorescence:** Dye (1 nmol per mouse) or HA-dye (1 nmol dye/mouse equivalent) in 80  $\mu$ L ultrapure water was intravenously injected into WT C57BL/6 mice or PDAC-bearing mice via tail vein (N = 5 mice/group). Mice were euthanized 24 h or 96 h post injection. WT mice were completely necropsied to examine overall fluorescence distribution of dye or dye conjugates. Dissected organs were imaged on a Pearl Trilogy small animal imaging system (LI-COR Biosciences, Lincoln, NE). The fluorescence intensity of each organ was collected with the 800 nm channel and analyzed with Image Studio Ver. 5.0 software (LI-COR Biosciences, Lincoln, NE). The periphery of each organ was identified by manually-defining the region of interest (ROI). Average pixel intensity was used to calculate SNR, which is defined by average tissue intensity per pixel in an ROI: standard deviation of background ROI.

**Simulated fluorescence guided imaging of PDAC:** Using the aforementioned dose, time, and contrast agents, mice were administered NIR fluorophore or HA-NIRF dye conjugates. After euthanasia, but prior to intraoperative imaging, the liver and spleen were removed to expose the pancreas and minimize background interference of those contrast agents cleared by the RES. A custom-designed FIGS system was employed to detect contrast enhancement of dye and HA-dye in the pancreatic tumors. The imaging system utilizes a handheld fiber-coupled

spectroscopic unit that emits an excitation laser at 785 nm and collects wavelength-resolved NIR emission (DeltaNu; Laramie, WY). The spectroscopic unit also serves as the excitation source for a real-time widefield imaging system (SpectroPath; Atlanta, GA, USA) that merges a NIR channel (800-950 nm) and a visible color channel for spatial orientation of the NIR signal. The overall design and integration of these systems has been previously reported [79]. A laser power of 80 mW at 785 nm was used for wavelength-resolved (800-950 nm) and widefield imaging.

After FIGS, all mice were necropsied. The pancreas was removed *en bloc* to preserve the anatomical integrity of the primary, stromal, and healthy tissues for fluorescence imaging (using the method described for WT mice) and histological sectioning. To compare against the intraoperative imaging analysis of each pancreas that was obtained during surgery, a straight line was drawn longitudinally across the pancreas in the image obtained by the Pearl Trilogy imaging system. The NIRF intensity along the line was quantified with the *plot profile* function in ImageJ 1.49v software (National Institutes of Health, Bethesda, MD). Tumor-bearing pancreata were directly compared against WT pancreata for all contrast agents.

A simulated surgical procedure was performed to evaluate tumor contrast with RES organs present in the surgical cavity. HA<sub>20k</sub>-NIRF dye conjugates (equivalent to 1 nmol of Cy7.5 or 10 nmol of IRDye800 per mouse) were administered to PDAC-bearing C57BL/6 mice for the acquisition of whole-body images. Mice were euthanized 24 h post injection. Wide-field imaging was acquired with two intraoperative imaging systems. A Lab-FLARE® RP1 small animal imaging system (Curadel, Marlborough, MA) compacted with whole-body excitation source and  $\approx$  800 nm NIRF emission was employed for the simultaneous determination of fluorescence from PDAC and surrounded abdominal organs. The overall design and operation of this system have been previously reported [80]. The Lab-FLARE® imaging system was also utilized to record videos. Exposure time of 150 ms and 12 ms were used for the NIRF laser and white light across all experimental groups, respectively. To confirm the fluorescence mapping, FDA-approved Fluobeam® 800 imaging system (Fluoptics, Cambridge, MA) was employed for whole-body NIRF imaging. The imaging system excites with a 780-nm emission laser and records with a CCD camera with >800 nm emission filtering. The exposure time of the NIRF laser was set to 100 ms and was consistent across all experimental groups.

**Histological analysis:** Tumor tissue was embedded in OCT mounting media gel and was rapidly frozen in liquid nitrogen (**Figure 5, S8**) for subsequent staining with H&E or left unstained for NIRF microscopy. Pancreatic tissue was positioned to obtain a maximal footprint for both diseased and healthy pancreases. These samples were cut with a cryostat (Leica Biosciences, Buffalo Grove, IL) at a thickness of 8  $\mu\text{m}$ . For immunohistological staining (**Figure 7, S8**), the pancreas was fixed with 4% paraformaldehyde solution for 24 h followed with 70% ethanol. Samples were embedded in wax and sectioned sequentially for immunohistological and H&E staining. Anti-CD44 antibody (Abcam, ab112178, Cambridge, MA) was applied at a dilution of 1:100. Anti-Ki67 antibody (Abcam, ab16667, Cambridge, MA) was applied at a dilution of 1:200. Representative unstained slides were scanned with Odyssey Clx imaging system (LI-COR, Lincoln, NE) with 800 nm channel. Exposure time was consistent among each group (HA-Cy7.5 and HA-IRDye800). H&E-stained slides were scanned with Panoramic 250 flash series digital scanner (3DHitech, Hungary). Representative microscopic photos for IHC and H&E were imaged and captured with an IX73 Inverted Microscope equipped with a DP80 Digital Camera and displayed by CellSens Dimension 1.13 software (all from Olympus, Japan).

**Statistical Analysis:** Data was analyzed with Prism 7 software (Graphpad, La Jolla, CA). Biodistribution and background interference were analyzed using a two-way ANOVA and Dunnett's multiple comparisons test; *ex vivo* analysis of contrast within pancreas was analyzed using one-way ANOVA with Tukey's multiple comparisons test; all data is shown as mean  $\pm$  standard deviation (SD).

## Abbreviations

BSA: bovine serum albumin; CNR: contrast-to-noise ratio; Cy7.5: Cyanine 7.5; DMSO: dimethyl sulfoxide; EDC: 1-Ethyl-3-(3-dimethylaminopropyl)-carbodiimide; FC: flow cytometry; HA: hyaluronic acid; HMW: high molecular weight; HP: healthy pancreas; ICG: indocyanine green; KPC: KPC (LSL-Kras<sup>G12D/+</sup>, LSL-Trp53<sup>R172H/+</sup>, Pdx-1Cre); LMW: low molecular weight; MW<sub>N</sub>: molecular weight; NHS: N-hydroxysuccinimide; NIRF: near infrared fluorescent; PDAC: pancreatic ductal adenocarcinoma; PPE: primary pancreatic epithelial; RES: reticuloendothelial system; ROI: region of interest; SEC: size exclusion chromatography; SNR: signal-to-noise ratio; UP: uninvolved pancreas; WT: wide type.

## Supplementary Material

Supplementary figures, tables, and video legends.

<http://www.thno.org/v10p3413s1.pdf>

Supplementary video 1.

<http://www.thno.org/v10p3413s2.mp4>

Supplementary video 2.

<http://www.thno.org/v10p3413s3.mp4>

Supplementary video 3.

<http://www.thno.org/v10p3413s4.mp4>

## Acknowledgements

We thank Megan B. Holmes and Dr. Joshua J. Soucek for generous help with mice handling, intraoperative IGS detection and necropsy. We also thank Ziling Zhao for assisting with FC data collection. Thomas C. Caffrey and Kelly A. O'Connell provided technical support for the orthotopic pancreatic cancer model. We also thank Tom Bargar for assisting with TEM imaging. We thank UNMC Flow Cytometry Core facility and UNMC Tissue Science Core Facility for instruction on FC data acquisition and analysis and sectioning and staining of pancreatic tissue. This work was supported in part by the National Institutes of Health [grant numbers R00CA153916, R01EB019449, P50CA127297, P20GM103480, U01CA210240, 1S10RR17846, 1S10RR027940, and P30CA036727 (Fred and Pamela Buffett Cancer Center at UNMC)], the Nebraska Cattlemen's Ball Development Fund, and the Nebraska Research Initiative.

## Competing interests

AMM is a co-inventor of the hand-held image-guided surgery system, which has been licensed to SpectroPath, Inc (Atlanta, GA).

## References

- Garrido-Laguna I, Hidalgo M. Pancreatic cancer: from state-of-the-art treatments to promising novel therapies. *Nat Rev Clin Oncol*. 2015; 12: 319–34.
- Vahrmeijer AL, Hutteman M, van der Vorst JR, van de Velde CJH, Frangioni J V. Image-guided cancer surgery using near-infrared fluorescence. *Nat Rev Clin Oncol*. 2013; 10: 507–18.
- Bao K, Lee JH, Kang H, Park GK, El Fakhri G, Choi HS. PSMA-targeted contrast agents for intraoperative imaging of prostate cancer. *Chem Commun (Camb)*. 2017; 53: 1611–4.
- Derks YHW, Löwik DWPM, Sedelaar JPM, et al. PSMA-targeting agents for radio- And fluorescence-guided prostate cancer surgery. *Theranostics*. 2019; 9: 6824–39.
- Wei R, Jiang G, Lv MQ, et al. TMTP1-modified indocyanine green-loaded polymeric micelles for targeted imaging of cervical cancer and metastasis sentinel lymph node in vivo. *Theranostics*. 2019; 9: 7325–44.
- Tummers WS, Miller SE, Teraphongphom NT, et al. Detection of visually occult metastatic lymph nodes using molecularly targeted fluorescent imaging during surgical resection of pancreatic cancer. *HPB (Oxford)*. 2019; 21: 883–90.
- Hoogstins CES, Boogerd LSF, Sibinga Mulder BG, et al. Image-Guided Surgery in Patients with Pancreatic Cancer: First Results of a Clinical Trial Using SGM-101, a Novel Carcinoembryonic Antigen-Targeting, Near-Infrared Fluorescent Agent. *Ann Surg Oncol*. 2018; 25: 3350–7.
- Nagaya T, Nakamura YA, Choyke PL, Kobayashi H. Fluorescence-Guided Surgery. *Front Oncol*. 2017; 7: 314.
- Hernot S, van Manen L, Debie P, Mieog JSD, Vahrmeijer AL. Latest developments in molecular tracers for fluorescence image-guided cancer surgery. *Lancet Oncol*. 2019; 20: e354–67.

10. Owens EA, Henary M, El Fakhri G, Choi HS. Tissue-Specific Near-Infrared Fluorescence Imaging. *Acc Chem Res.* 2016; 49: 1731–40.
11. Owens EA, Lee S, Choi J, Henary M, Choi HS. NIR fluorescent small molecules for intraoperative imaging. *Wiley Interdiscip Rev Nanomedicine Nanobiotechnology.* 2015; 7: 828–38.
12. Ye Y, Chen X. Integrin targeting for tumor optical imaging. *Theranostics.* 2011; 1: 102–26.
13. Achilefu S. The Insatiable Quest for Near-Infrared Fluorescent Probes for Molecular Imaging. *Angew Chemie Int Ed.* 2010; 49: 9816–8.
14. Ballou B, Fisher GW, Waggoner AS, et al. Tumor labeling in vivo using cyanine-conjugated monoclonal antibodies. *Cancer Immunol Immunother.* 1995; 41: 257–63.
15. Choi HS, Nasr K, Alyabyev S, et al. Synthesis and In Vivo Fate of Zwitterionic Near-Infrared Fluorophores. *Angew Chemie Int Ed.* 2011; 50: 6258–63.
16. Choi HS, Gibbs SL, Lee JH, et al. Targeted zwitterionic near-infrared fluorophores for improved optical imaging. *Nat Biotechnol.* 2013; 31: 148–53.
17. Barstow L, Small RE. Liver Function Assessment by Drug Metabolism. *Pharmacother J Hum Pharmacol Drug Ther.* 1990; 10: 280–8.
18. Choi HS, Liu W, Liu F, et al. Design considerations for tumour-targeted nanoparticles. *Nat Nanotechnol.* 2010; 5: 42–7.
19. Choi HS, Misra P, Bawendi MG, et al. Renal clearance of quantum dots. *Nat Biotechnol.* 2007; 25: 1165–70.
20. Becker A, Hesselius C, Licha K, et al. Receptor-targeted optical imaging of tumors with near-infrared fluorescent ligands. *Nat Biotechnol.* 2001; 19: 327–31.
21. Ntziachristos V, Bremer C, Weissleder R. Fluorescence Imaging With Near-Infrared Light: New Technological Advances That Enable In Vivo Molecular Imaging. *Eur Radiol.* 2003; 13: 195–208.
22. Hiroshima Y, Maawy A, Sato S, et al. Hand-held high-resolution fluorescence imaging system for fluorescence-guided surgery of patient and cell-line pancreatic tumors growing orthotopically in nude mice. *J Surg Res.* 2014; 187: 510–7.
23. Nguyen QT, Olson ES, Aguilera TA, et al. Surgery with molecular fluorescence imaging using activatable cell-penetrating peptides decreases residual cancer and improves survival. *Proc Natl Acad Sci U S A.* 2010; 107: 4317–22.
24. Bao K, Nasr KA, Hyun H, et al. Charge and hydrophobicity effects of NIR fluorophores on bone-specific imaging. *Theranostics.* 2015; 5: 609–17.
25. Hill TK, Abdulahad A, Kelkar SS, et al. Indocyanine green-loaded nanoparticles for image-guided tumor surgery. *Bioconjug Chem.* 2015; 26: 294–303.
26. Hill T, Kelkar S, Wojtynek N, Soucek J. Near Infrared Fluorescent Nanoparticles Derived from Hyaluronic Acid Improve Tumor Contrast for Image-Guided Surgery. *Theranostics.* 2016; 6: 2314–28.
27. Mohs AM, Soucek JJ, Holmes MB, et al. Hyaluronic acid formulation of near infrared fluorophores optimizes surgical imaging in a prostate tumor xenograft. *Acta Biomater.* 2018; 75: 323–33.
28. Qi B, Crawford AJ, Wojtynek NE, et al. Indocyanine green loaded hyaluronan-derived nanoparticles for fluorescence-enhanced surgical imaging of pancreatic cancer. *Nanomedicine Nanotechnology, Biol Med.* 2018; 14: 769–80.
29. Kelkar S, Hill T, Marini F MA, Kelkar SS, Hill TK, Marini FC, Mohs AM. Near infrared fluorescent nanoparticles based on hyaluronic acid: Self-assembly, optical properties, and cell interaction. *Acta Biomater.* 2016; 36: 112–21.
30. Tatikolov AS, Costa SMB. Effects of normal and reverse micellar environment on the spectral properties, isomerization and aggregation of a hydrophilic cyanine dye. *Chem Phys Lett.* 2001; 346: 233–40.
31. v. Berlepsch H, Böttcher C. H-Aggregates of an Indocyanine Cy5 Dye: Transition from Strong to Weak Molecular Coupling. *J Phys Chem B.* 2015; 119: 11900–9.
32. Würthner F, Kaiser TE, Saha-Möllner CR. J-Aggregates: From Serendipitous Discovery to Supramolecular Engineering of Functional Dye Materials. *Angew Chemie Int Ed.* 2011; 50: 3376–410.
33. Chen D, Ganesh S, Wang W, Amiji M. Plasma protein adsorption and biological identity of systemically administered nanoparticles. *Nanomedicine.* 2017; 12: 2113–35.
34. Berezin MY, Guo K, Akers W, et al. Rational Approach To Select Small Peptide Molecular Probes Labeled with Fluorescent Cyanine Dyes for in Vivo Optical Imaging. *Biochemistry.* 2011; 50: 2691–700.
35. Almalik A, Benabdelkamel H, Masood A, et al. Hyaluronic Acid Coated Chitosan Nanoparticles Reduced the Immunogenicity of the Formed Protein Corona. *Sci Rep.* 2017; 7: 10542.
36. Ramadan MH, Prata JE, Karácsony O, Dunér G, Washburn NR. Reducing Protein Adsorption with Polymer-Grafted Hyaluronic Acid Coatings. *Langmuir.* 2014; 30: 7485–95.
37. Levesque E, Martin E, Dudau D, Lim C, Dhonneur G, Azoulay D. Current use and perspective of indocyanine green clearance in liver diseases. *Anaesth Crit Care Pain Med.* 2016; 35: 49–57.
38. Schaafsma BE, Mieog JSD, Hutteman M, et al. The clinical use of indocyanine green as a near-infrared fluorescent contrast agent for image-guided oncologic surgery. *J Surg Oncol.* 2011; 104: 323–32.
39. Hamann FM, Brehm R, Pauli J, et al. Controlled Modulation of Serum Protein Binding and Biodistribution of Asymmetric Cyanine Dyes by Variation of the Number of Sulfonate Groups. *Mol Imaging.* 2011; 10: 258–269.
40. Berezin MY, Lee H, Akers W, Nikiforovich G, Achilefu S. Ratiometric Analysis of Fluorescence Lifetime for Probing Binding Sites in Albumin with Near-Infrared Fluorescent Molecular Probes. *Photochem Photobiol.* 2007; 83: 1371–8.
41. Tian R, Zeng Q, Zhu S, et al. Albumin-chaperoned cyanine dye yields superbright NIR-II fluorophore with enhanced pharmacokinetics. *Sci Adv.* 2019; 5: eaaw0672.
42. Beckford G, Owens E, Henary M, Patonay G. The solvatochromic effects of side chain substitution on the binding interaction of novel tricyanobocyanine dyes with human serum albumin. *Talanta.* 2012; 92: 45–52.
43. Mérian J, Boisgard R, Bayle P-A, Bardet M, Tavitian B, Texier I. Comparative biodistribution in mice of cyanine dyes loaded in lipid nanoparticles. *Eur J Pharm Biopharm.* 2015; 93: 1–10.
44. Castano AP, Demidova TN, Hamblin MR. Mechanisms in photodynamic therapy: Part three—Photosensitizer pharmacokinetics, biodistribution, tumor localization and modes of tumor destruction. *Photodiagnosis Photodyn Ther.* 2005; 2: 91–106.
45. Alexis F, Pridgen E, Molnar LK, Farokhzad OC. Factors Affecting the Clearance and Biodistribution of Polymeric Nanoparticles. *Mol Pharm.* 2008; 5: 505–15.
46. Hilderbrand SA, Weissleder R. Near-infrared fluorescence: application to in vivo molecular imaging. *Curr Opin Chem Biol.* 2010; 14: 71–9.
47. Hoshyar N, Gray S, Han H, Bao G. The effect of nanoparticle size on in vivo pharmacokinetics and cellular interaction. *Nanomedicine (Lond).* 2016; 11: 673–92.
48. Qiu LY, Bae YH. Polymer Architecture and Drug Delivery. *Pharm Res.* 2006; 23: 1–30.
49. Courel M-N, Maingonnat C, Bertrand P, Chauzy C, Smadja-Joffe F, Delpach B. Biodistribution of injected tritiated hyaluronic acid in mice: a comparison between macromolecules and hyaluronic acid-derived oligosaccharides. *In vivo (Athens, Greece).* 2004; 18: 181–7.
50. Mohs AM, Mancini MC, Singhal S, et al. Hand-held spectroscopic device for in vivo and intraoperative tumor detection: Contrast enhancement, detection sensitivity, and tissue penetration. *Anal Chem.* 2010; 82: 9058–65.
51. Arami H, Khandhar A, Liggett D, Krishnan KM. In vivo delivery, pharmacokinetics, biodistribution and toxicity of iron oxide nanoparticles. *Chem Soc Rev.* 2015; 44: 8576–607.
52. Yang Z, Leon J, Martin M, et al. Pharmacokinetics and biodistribution of near-infrared fluorescence polymeric nanoparticles. *Nanotechnology.* 2009; 20: 165101.
53. Thompson M, Nel AE, Somasundaran P, et al. Understanding biophysicochemical interactions at the nano-bio interface. *Nat Mater.* 2009; 8: 543–57.
54. Kamaly N, He JC, Ausiello DA, Farokhzad OC. Nanomedicines for renal disease: current status and future applications. *Nat Rev Nephrol.* 2016; 12: 738–53.
55. Vearborough A, Passirani C, Saulnier P, Benoit J-P. Parameters influencing the stealthiness of colloidal drug delivery systems. *Biomaterials.* 2006; 27: 4356–73.
56. Grabolle M, Pauli J, Brehm R, Resch-Genger U. Structural control of dye-protein binding, aggregation and hydrophilicity in a series of asymmetric cyanines. *Dye Pigment.* 2014; 103: 118–26.
57. Iyer AAK, Khaled G, Fang J, Maeda H. Today HM-D discovery, 2006 U. Exploiting the enhanced permeability and retention effect for tumor targeting. *drug discov today.* 2006; 11: 812–8.
58. Rhim AD, Oberstein PE, Thomas DH, et al. Stromal Elements Act to Restrain, Rather Than Support, Pancreatic Ductal Adenocarcinoma. *Cancer Cell.* 2014; 25: 735–47.
59. Taurin S, Nehoff H, Release KG-J of controlled, 2012 U. Anticancer nanomedicine and tumor vascular permeability; where is the missing link? *J Control Release.* 2012; 164: 265–75.
60. Cabral H, Matsumoto Y, Mizuno K, et al. Accumulation of sub-100 nm polymeric micelles in poorly permeable tumours depends on size. *Nat Nanotechnol.* 2011; 6: 815–23.
61. Kuehl C, Zhang T, Kaminskas LM, et al. Hyaluronic Acid Molecular Weight Determines Lung Clearance and Biodistribution after Instillation. *Mol Pharm.* 2016; 13: 1904–14.
62. Matsumoto Y, Nichols JJW, Toh K, et al. Vascular bursts enhance permeability of tumour blood vessels and improve nanoparticle delivery. *Nat Nanotechnol.* 2016; 11: 533–8.
63. DuFort CCC, DelGiorno KKE, Carlson MA, et al. Interstitial pressure in pancreatic ductal adenocarcinoma is dominated by a gel-fluid phase. *Biophys J.* 2016; 110: 2106–19.
64. Itano N, Zhuo L, Kimata K. Impact of the hyaluronan-rich tumor microenvironment on cancer initiation and progression. *Cancer Sci.* 2008; 99: 1720–5.
65. Sato N, Koshi S, Hirata K, Goggins M. Role of hyaluronan in pancreatic cancer biology and therapy: Once again in the spotlight. *Cancer Sci.* 2016; 107: 569–75.
66. Lesley J, Hascall V, Tammi M, Chemistry RH-J of B, 2000 U. Hyaluronan binding by cell surface CD44. *J Biol Chem.* 2000; 275: 26967–75.
67. Te Velde E, Veerman T, Subramaniam V, Ruers T. The Use of Fluorescent Dyes and Probes in Surgical Oncology. *Eur J Surg Oncol.* 2010; 36: 6–15.
68. Yan H, Siesler HW. Quantitative analysis of a pharmaceutical formulation: Performance comparison of different handheld near-infrared spectrometers. *J Pharm Biomed Anal.* 2018; 160: 179–86.

69. Judy RP, Keating JJ, Dejesus EM, et al. Quantification of tumor fluorescence during intraoperative optical cancer imaging. *Sci Rep.* 2015; 5: 16208.
70. Zhao S, Chen C, Chang K, et al. CD44 Expression Level and Isoform Contributes to Pancreatic Cancer Cell Plasticity, Invasiveness, and Response to Therapy. *Clin Cancer Res.* 2016; 22: 5592–604.
71. Wood NJ. Pancreatic cancer: pancreatic tumour formation and recurrence after radiotherapy are blocked by targeting CD44. *Nat Rev Gastroenterol Hepatol.* 2014; 11: 73
72. Li X, Zhang X, Zheng L, Guo W. Expression of CD44 in pancreatic cancer and its significance. *Int J Clin Exp Pathol.* 2015; 8: 6724–31.
73. Hong SP, Wen J, Bang S, Park S, Song SY. CD44-positive cells are responsible for gemcitabine resistance in pancreatic cancer cells. *Int J Cancer.* 2009; 125: 2323–31.
74. Takaishi S, Okumura T, Tu S, et al. Identification of Gastric Cancer Stem Cells Using the Cell Surface Marker CD44. *Stem Cells.* 2009; 27: 1006–20.
75. Hsu C, Lee L, Hsu J, et al. CD44 Predicts Early Recurrence in Pancreatic Cancer Patients Undergoing Radical Surgery. *In Vivo.* 2018; 32: 1533–40.
76. Torres MP, Rachagani S, Soucek JJ, Mallya K, Johansson SL, Batra SK. Novel pancreatic cancer cell lines derived from genetically engineered mouse models of spontaneous pancreatic adenocarcinoma: applications in diagnosis and therapy. *PLoS One.* 2013; 8: e80580.
77. Watanabe M, Sheriff S, Lewis KB, et al. Metabolic Profiling Comparison of Human Pancreatic Ductal Epithelial Cells and Three Pancreatic Cancer Cell Lines using NMR Based Metabonomics. *J Mol Biomark Diagn.* 2012; 3.
78. Tsutsumida H. RNA Interference Suppression of MUC1 Reduces the Growth Rate and Metastatic Phenotype of Human Pancreatic Cancer Cells. *Clin Cancer Res.* 2006; 12: 2976–87.
79. Mohs A, Mancini M, Provenzale J, et al. An integrated widefield imaging and spectroscopy system for contrast enhanced, image-guided research of tumors. *IEEE Trans Biomed Eng.* 2015; 62: 1416–24.
80. Troyan SL, Kianzad V, Gibbs-Strauss SL, et al. The FLARE™ Intraoperative Near-Infrared Fluorescence Imaging System: A First-in-Human Clinical Trial in Breast Cancer Sentinel Lymph Node Mapping. *Ann Surg Oncol.* 2009; 16: 2943–52.